Front. Mech. Eng. 2024, 19(4): 24
https://doi.org/10.1007/s11465-024-0795-1

RESEARCH ARTICLE

Efficient measurement and optical proximity correction modeling to catch lithography pattern shift issues of arbitrarily distributed hole layer

Yaobin FENG[a‡], Jiamin LIU (✉)[a‡], Zhiyang SONG[a], Jiang HAO (✉)[a], Shiyuan LIU[a,b]

[a] *State Key Laboratory of Intelligent Manufacturing Equipment and Technology, Huazhong University of Science and Technology, Wuhan 430074, China*
[b] *Optics Valley Laboratory, Wuhan 430074, China*
✉ *Corresponding authors. E-mails: jiaminliu@hust.edu.cn (Jiamin LIU); hjiang@hust.edu.cn (Hao JIANG)*

ABSTRACT With the continued shrinking of the critical dimensions (CDs) of wafer patterning, the requirements for modeling precision in optical proximity correction (OPC) increase accordingly. This requirement extends beyond CD controlling accuracy to include pattern alignment accuracy because misalignment can lead to considerable overlay and metal-via coverage issues at advanced nodes, affecting process window and yield. This paper proposes an efficient OPC modeling approach that prioritizes pattern-shift-related elements to tackle the issue accurately. Our method integrates careful measurement selection, the implementation of pattern-shift-aware structures in design, and the manipulation of the cost function during model tuning to establish a robust model. Confirmatory experiments are performed on a via layer fabricated using a negative tone development. Results demonstrate that pattern shifts can be constrained within a range of ±1 nm, remarkably better than the original range of ±3 nm. Furthermore, simulations reveal notable differences between post OPC and original masks when considering pattern shifts at locations sensitive to this phenomenon. Experimental validation confirms the accuracy of the proposed modeling approach, and a firm consistency is observed between the simulation results and experimental data obtained from actual design structures.

KEYWORDS computational lithography, optical proximity correction, modeling, pattern shift, metrology

1 Introduction

Optical lithography is one of the indispensable processes in integrated circuit manufacturing and can transfer the pattern structures from the mask to the resist coated on the wafer. The most recent exposure system from ASML, the Netherlands, for high-volume manufacturing provides a resolution of around 13 nm half pitch, which is adequate for the 5 nm/3 nm logic nodes and leading-edge DRAM nodes. To take advantage of the sub-wavelength resolution of lithography sufficiently and acquire an adequate process window, various resolution enhancement techniques (RETs) have been developed to improve the imaging quality of the lithography system [1]. Among all the RETs, optical proximity correction (OPC) is the most widely employed technique at 0.25 μm and below nodes. OPC modifies the mask patterns to correct the aerial and resist images and compensate for the proximity effects of neighboring features, thereby improving the printability on the wafer. OPC constitutes the core part of computational lithography [2], which is an inclusive expression to describe modern lithography with tremendous calculations.

For decades, the semiconductor industry has adopted OPC to compensate for and minimize the imaging distortions of lithography systems. The OPC model mainly consists of the optical and resist parts [3]. The optical part is designed to simulate the aerial image and has been well-developed in the past by several electronic design automation companies and research organizations [4]. The resist part mainly describes the photochemical reactions during the exposure, the chemical reactions and diffusion phenomena during the post-exposure bake, and the development processing [5]. Although numerous resist models have been proposed and used in

Received April 26, 2024; accepted May 30, 2024; online July 22, 2024
‡ These authors contributed equally.

semiconductor industries for various simulations, actual OPC usually needs simplified resist models for fast simulation of full-chip areas. Because the threshold-based resist model has the advantages of a simple formula and easy numerical calculation [5,6], it is often widely used to integrate with aerial image models. The resist models based on a single-threshold truncating relative intensity to acquire resist images are the earliest photoresist models used by engineers and researchers [7]. Considering that the single-threshold resist model cannot predict the practical photoresist behavior for various patterns with sufficient accuracy, variable-threshold resist models emerged [8]. Subsequently, the compact resist model was proposed and served as the standard process model for OPC [9–12]. In addition to being widely adopted in OPC, the compact model has been used for the placement of model-based sub-resolution assist features (SRAFs) and the prediction of extra printing, including resist top loss and SRAF printing [13,14].

The compact model parameters are usually calibrated from the critical dimension (CD) measurements of typical test patterns. Advanced lithography and etch processes demand accurate, robust metrology solutions to characterize and control the CDs. The classical approach employs a high-resolution scanning electron microscope (SEM) to capture top-view grayscale images of representative structures. According to the internal algorithm adopted in the SEM tools, only a part of the image inside a measurement box is valid to extract the CD, which means some helpful information from the SEM image is lost [15]. As a result, the number of needed CD measurements is usually over 10000 for OPC models at advanced nodes [16]. To extract more valuable data and minimize the number of SEM measurements, an alternative method is to extract the edge contours inside the SEM image and acquire placement vectors instead of CDs for the calibration of OPC models, which is equivalent to substantial amounts of single CDs [17–21]. Thus, fewer images are needed to save the metrology tool time and work for data handling. The discussion and utilization of SEM image contours for OPC modeling purposes have continued for some time and have demonstrated additional benefits in two aspects. First, the SEM image contour represents the entire shape of the complicated 2D structures, which captures the complete information for more accurate OPC modeling. Second, the SEM image contour with a large field of view (FOV) keeps the mutual location information, indicating that the OPC modeling can accurately consider the pattern shift of adjacent structures. Even though the benefits of SEM image contours are apparent, several challenges remain when dealing with SEM image contours [22–24]. The first one lies in the difficulty of obtaining reliable contours and dealing with this type of data, which needs many strategies to improve the quality of SEM images and to reduce systematic errors such as anisotropic image contrast and image distortions. Related to the elaboration of the above issue, the averaging strategy of the contours from multiple images and the lousy image analysis is an unresolved fundamental problem. The second problem involving contour alignment has received the most attention so far. No broad discussion and demonstration of the solution is available, especially for substantial amounts and various kinds of test structures for OPC calibration. In addition, a perfect match between CDs obtained from direct wafer measurement and extracted contours is required to guarantee the same characteristic of edges from photoresist patterns. Bias between the measurements of one- and two-dimensional structures is another practical concern, promoting hybrid modeling with mixed CDs from wafers and contours from OPC.

This work addresses the challenge of accurately modeling pattern shifts without substantial compromise to the conventional precision requirement of CDs. As previously discussed, conventional only-CD-considered OPC modeling fails to capture this issue effectively due to the absence of relative location information. Although SEM contour-based metrology inherently incorporates such information, several factors can still undermine modeling precision. Therefore, a hybrid modeling approach integrating direct CD measurements with pattern shift data extracted from SEM images is proposed to mitigate potential risks. To enhance the reliability of pattern shift measurement, discussions and experiments on metrology are conducted to address the limitations of the current SEM contour extraction methods. Aerial image modeling and compact photoresist modeling are provided in Section 2. The metrology strategy and OPC modeling are presented in Section 3. Experimental details, including the modeling and simulation results compared with wafer verification, are outlined in Section 4. Finally, the conclusions and an outlook for future research directions are discussed in Section 5.

2 Aerial image model and compact resist model

The physical essence of the optical lithography is partial coherent imaging, and the resultant aerial image can be calculated using Hopkins theory with a transmission cross-coefficient (TCC) as follows [25]:

$$I(x,y)=\iint \mathrm{TCC}\left(f_x',f_y',f_x'',f_y''\right)\tilde{O}\left(f_x',f_y'\right)\tilde{O}^*\left(f_x'',f_y''\right)\cdot e^{-2\pi\mathrm{i}\left[\left(f_x'-f_x''\right)x+\left(f_y'-f_y''\right)y\right]}\mathrm{d}f_x'\mathrm{d}f_y'\mathrm{d}f_x''\mathrm{d}f_y'', \tag{1}$$

$$\mathrm{TCC}\left(f_x',f_y',f_x'',f_y''\right)=\iint J\left(f_x,f_y\right)H\left(f_x+f_x',f_y+f_y'\right)\cdot H\left(f_x+f_x'',f_y+f_y''\right)\mathrm{d}f_x\mathrm{d}f_y, \tag{2}$$

where $I(x, y)$ represents the normalized aerial image of the photomask pattern. Variable pairs (f_x, f_y), (f_x', f_y'), and

(f_x'', f_y'') are the coordinates in the spatial-frequency domain, and variable pair (x, y) represents the coordinates in the spatial domain. $\hat{O}(f_x', f_y')$ is the spectrum of mask patterns in the frequency domain, and $\hat{O}(f_x'', f_y'')$ is the corresponding complex conjugate. $J(f_x, f_y)$ and $H(f_x, f_y)$ represent the illumination and imaging pupils of the lithography imaging system, respectively. After decomposing the TCC into a series of partially coherent kernels, the aerial image can be expressed in a more calculation-friendly form as follows:

$$I(x,y) = \sum_{i=1}^{N} \lambda_i |\Phi_i(x,y) \otimes O(x,y)|^2, \tag{3}$$

where the kernels $\Phi_i(x, y)$ is a series of orthogonal eigenfunctions in the space domain. The operator $\otimes$ represents the 2D convolution, and N is the number of eigenfunctions. Coefficient λ_i is the ith eigenvalue corresponding to the ith eigenfunction $\Phi_i(x, y)$.

The compact resist model currently serves as the standard model used in the OPC industry. This model is based on the above-mentioned aerial imaging model and is used to optimize the photoresist parameters to acquire the resist contours at the specific height of the resist profile. The resist image on the wafer surface can be expressed by a linear combination of different modeling terms $M_i(x, y)$. The general form of the compact resist model can be defined as follows:

$$R(x,y) = \sum_{i=1}^{N} c_i M_i(x,y), \tag{4}$$

$$M_i(x,y) = \left\{ \left[\nabla^k I_{\mp b}(x,y) \right]^n \otimes G_{s,p}(x,y) \right\}^{1/n}, \tag{5}$$

where $R(x, y)$ denotes the photoresist image, and c_i is the coefficient of the ith modeling parameter. As mentioned above, $I(x, y)$ represents the aerial image, and b is the neutralization constant. The positive and negative signs are the acid and base neutralization, respectively. Coefficient k is the differentiation order, and $G(x, y)$ is the Gauss–Laguerre kernel. Subscripts s and p from the kernel are the order and diffusion length, respectively. The compact model theoretically has 2^N-1 kinds of model forms, where N represents the number of parameters [26]. Thus, the performance of the compact model fundamentally depends on the number of parameters involved in modeling. A typical compact model $R(x, y)$ involving eight model terms is presented as follows [27]:

$$\begin{aligned} R(x,y) = {} & c_0 I + c_1 I_{+b_1} \otimes G_{S_1} + c_2 I_{+b_2} \otimes G_{S_2} + c_3 I_{-b_3} \otimes G_{S_3} \\ & + c_4 |\nabla I| \otimes G_{S_4} + c_5 \left[I^2 \otimes G_{S_5} \right]^{0.5} + c_6 \left[I_{-b_6}^2 \otimes G_{S_6} \right]^{0.5} \\ & + c_7 \nabla^2 I \otimes G_{S_7} + \cdots, \end{aligned} \tag{6}$$

where these terms represent some modifications to the aerial images. $I_{\pm b_i}$ related terms represent base or acid neutralization and diffusion behaviors after truncation effects from quencher or other additives into the resist to improve the imaging performance. $\nabla^k I$ is the first or second derivative-related terms, representing imaging contrast-induced effects on the resist image.

Based on the wafer measurements and searching algorithm, the model calibration strategy is then proposed to optimize the model parameters. The optimized model from the calibration should not only reproduce those wafer CDs but also predict the contours of the actual layouts with high fidelity. Correspondingly, model calibration usually needs accurate wafer measurements, summarized as gauges. The CD gauge and the edge placement (EP) gauge are two typical gauges. The weighted root mean square (RMS) of model error on the measured gauges is the cost function for evaluating and optimizing the model performance. For the CD gauge, the model error is defined as the simulated CD minus corresponding wafer data. For the EP gauge, the model error is defined as the distance between a particular sampling point on the simulation contour and the corresponding point on the wafer contour.

$$\mathrm{RMS} = \sqrt{\frac{\sum_i wt_i \cdot e_{\mathrm{m},i}^2}{\sum_i wt_i}}, \tag{7}$$

where wt_i is the ith weight factor, and $e_{\mathrm{m},i}$ is the ith model error.

Compared with the conventional CD gauge, the EP gauge carries the location and contour shape information with a vector at the specific measurement position. The additional 2D and position information included in the EP gauge can be used to sense the effects of pattern shift. However, the EP gauge has higher requirements on metrology, mainly including high-quality images for reliable contour extraction, accurate die-to-database alignment for contour alignment with image, CD matching capability to ensure consistency with inline CD metrology, and massive data handling capabilities. Therefore, to avoid excess expense on OPC modeling, the methodology for accurately modeling pattern shifts without the EP gauge is meaningful. In this work, apart from EP gauge, gauges from CD and space are included in the modeling. The difference in CD accuracy and prediction of pattern shift between calibrated models is checked to verify if the CD gauge can model the pattern shifts equally. The spaces are especially selected to ensure the measurement is reliable and can contain information relative to pattern shift, which will be demonstrated in the following section.

3 Proposed metrology and modeling strategy

To evaluate the scope of a pattern shift, pitch patterns with CD and pitch similar to the real-chip structures are designed, as shown in Fig. 1.

Each pitch of all the test patterns is measured

sequentially from left to right to check the range that the optical proximity-induced pattern shift affects and the distance of its influence. When collecting the SEM image data, the classical SEM measurement is based on a small FOV with a range of around 500 nm to acquire reasonable accuracy. In comparison, the maximum pitch of selected structures is around 1000 nm, depending on the optical diameter (OD) of OPC modeling. Different SEM tools and settings are evaluated to determine the strategy for enlarging the FOV of data collection in our work. Only the most central pitch of the through-pitch patterns is collected to demonstrate the effect of metrology on the measurement. As shown in Fig. 2, the x axis represents the test patterns' target pitch, and the y axis represents the error between measurement and target pitches. Some distortion related to the distance is observed by measuring pitch. After proper selection and modification of the SEM settings, the absolute error of pitch measurement could be minimized, with around 1.2 nm per thousand nanometers shrunk from 3.9 nm per thousand nanometers.

Then, the pitch data of the through-pitch array structure from left to right are collected for the study. Each row and column of data from the array are collected and shown separately in Fig. 3. The x axis indicates the number of pitches from left to right, and the y axis shows the bias of the measured pitch against the target pitch. Corresponding pitches from each array row are averaged to gain more robust data. Based on the experimental results from typical patterns as shown below, the pattern

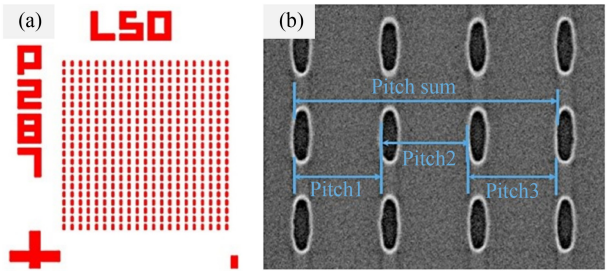

Fig. 1 (a) Designed array structure for pattern match measurement and (b) SEM image.

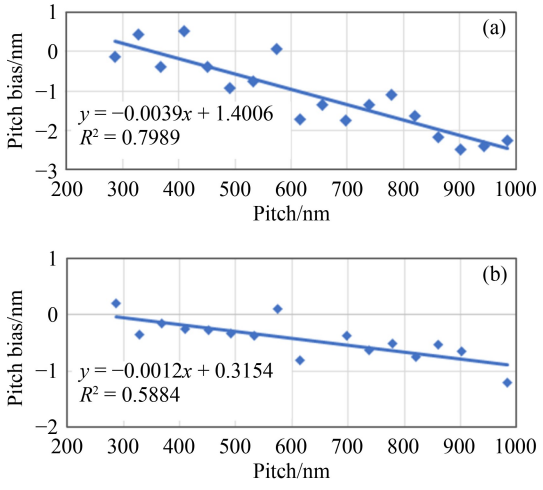

Fig. 2 (a–b) Error analysis of pitch measurement from two SEM settings.

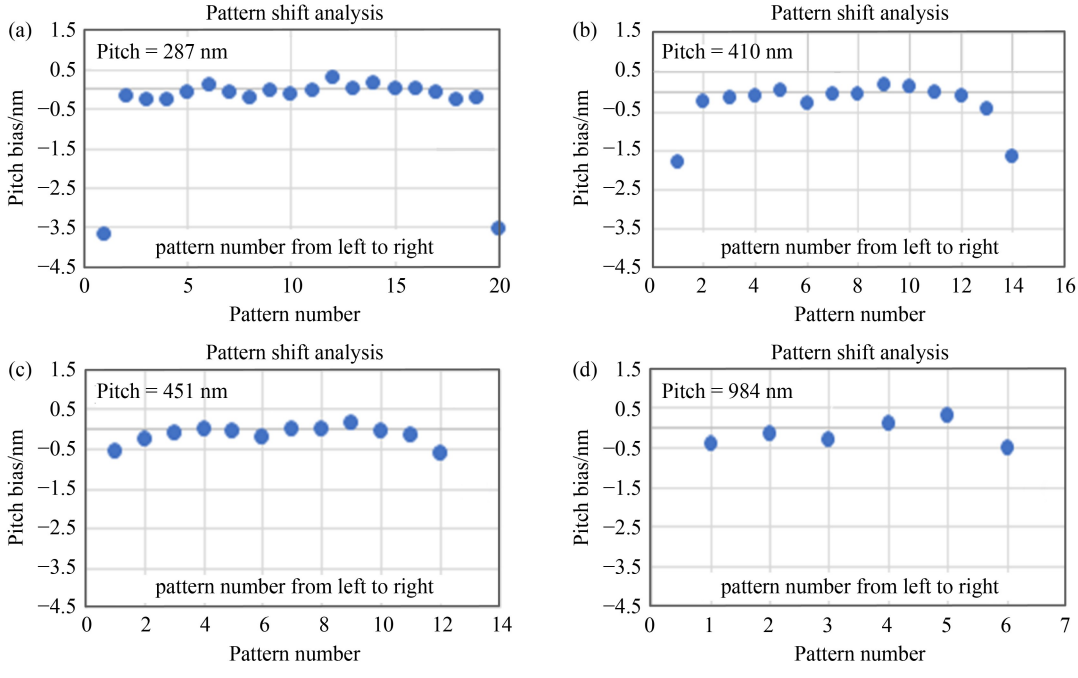

Fig. 3 Pattern shift data from the array's left edge to its right edge under different pitches: pitches of (a) 287, (b) 410, (c) 451, and (d) 984 nm. Extreme edges with substantial shift can be observed at (a) and (b).

shift mainly exists at the edge of the array, and the value decays from around 3.5 to around 0.5 nm as the pitch size grows from 287 to more than 451 nm. The results demonstrate a remarkable relationship between the pattern shift and the optical proximity effect. Closer patterns interact with one another more apparently, and the effective distance coincides with the OD, underlying the effect as the optical domain. However, the array patterns are compensated for through a simple OPC model calibrated from a small number of CD gauges, which means the absence of relative location information could result in the negligence of pattern shift. A compact model without a proper sampling of the relative location cannot forecast the effect precisely even though the phenomenon is optical dominating.

To demonstrate the pattern shift from the OPC modeling, a beta-version model is calibrated with the CD gauge collected previously from the OPC test mask based on the aerial imaging and compact modeling methodology in Section 2. The aerial and resist images of the first three patterns from Fig. 3 are shown in Fig. 4. The *x* axis is the relative location from the start point of the simulation region. The *y* axis is the relative intensity of the image. Although the aerial and resist images have the same *y* axis, the normalization bases differ. Thus, the gap between the aerial and resist image intensities does not make much sense. The intensities of the four most edge patterns are presented, and the substantial difference in distance between the first three patterns and the last one considers the center of intensity, which indicates the center of patterns from a couple of patterns at the edge of the aerial image. The results indicate the pattern shift mainly comes from the optical effects at locations with different surroundings. The difference of centers is also marked from the aerial image and resist image, which shows a progressively smaller bias along with pitch growth. Compared with actual wafer data, the compact photoresist model tries to capture the effect, but the result is suboptimal because no information on pattern shift is included in the modeling.

To include the effect in modeling, an FOV of 1200 nm is selected considering the measurement distortion and effective distance of pattern shift, which means a radius of 600 nm. Besides the CD data from the hole, the space data that combines with CD data is collected to form a pitch at the array edges to describe the information of pattern shift. Only spaces less than 500 nm are counted in the model calibration to minimize the systematic distortion. However, space gauge is fewer compared with the CD gauge. The number of the space gauge is 13, whereas the number of the CD gauge is around 600. To emphasize the space information during the calibration of

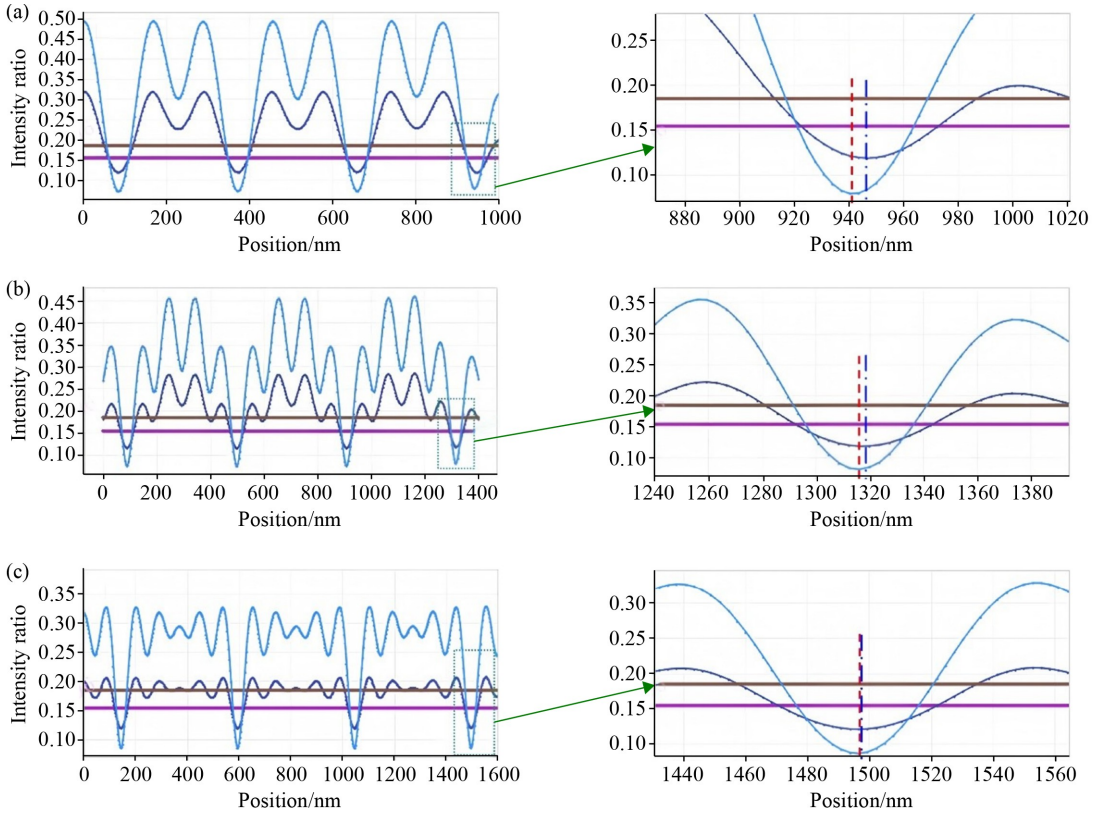

Fig. 4 Intensity distribution of aerial image (higher intensity and threshold) and resist image (lower intensity and threshold) at the extreme edge of different pitches: pitches of (a) 287, (b) 410, and (c) 451 nm.

the model, the cost function of modeling is modified by assigning independent weights to the group of space gauge.

$$\mathrm{RMS}_{\mathrm{new}} = \sqrt{\frac{\sum_i wt_i \cdot e_{\mathrm{CD},i}^2}{\sum_i wt_i} + wt_{\mathrm{space}} \frac{\sum_j wt_j \cdot e_{\mathrm{SP},j}^2}{\sum_j wt_j}}, \quad (8)$$

where wt_{space} is the weight factor for the space gauge, $e_{\mathrm{CD},i}$ represents the ith error corresponding to the CD gauge, and $e_{\mathrm{SP},j}$ represents the jth error corresponding to the space gauge.

Besides modifying the cost function mentioned above, a contour-based method is employed to extract the EP gauge from the SEM images through the metrology of extreme performance technique [28], and a commercial software tool is used for SEM contour extraction and analysis. The benefit of the SEM image contour is evident. The space information is natively contained in the EP gauge. Carefully balancing the normalized weights of CD and space is not needed. Additional work on CD matching and GDS-to-database alignment is needed to extract reliable EP gauges for modeling. In this case, the CD matching is implemented through pitch patterns of line-space and design-like structures depending on the industry methodology. The difference between measurements of the wafer and contour is within 0.3 nm, which is acceptable. Notably, the alignment is mainly based on the total displacement method [24], which could minimize the distance between corresponding sampling points within the effective FOV. The scheme can average the pattern shift of adjacent structures to all the patterns in FOV. Thus, the selection of images for extracting contours of pattern shift should be carefully designed and reviewed after the alignment. As shown in Fig. 5, the SEM image in Fig. 5(a) is unsuitable for EP gauge extraction because the shift makes distinguishing between patterns difficult. The SEM image in Fig. 5(b) provides reliable shift data at the extreme edges because many sampling points without substantial shifts provide an anchor to measure the change.

The two types of pattern-shift data are collected and meticulously cleaned in preparation for modeling. Classical compact modeling, in which various parameters are involved in convolution, is employed. A genetic algorithm is employed to optimize multiple parameters and attain global optimal solutions. Additionally, to leverage the EP gauges fully, machine learning (ML)-based modeling is incorporated as a reference [29]. However, the authors refrain from selecting the ML model as the baseline for tape-out due to the limited data, which poses a risk of overfitting during calibration. Three models, each representing a different combination, are calibrated: classical modeling with gauges of CDs and spaces, classical modeling with the EP gauge, and ML modeling with the EP gauge. These models are calibrated to capture the pattern shifts, and subsequent comparisons

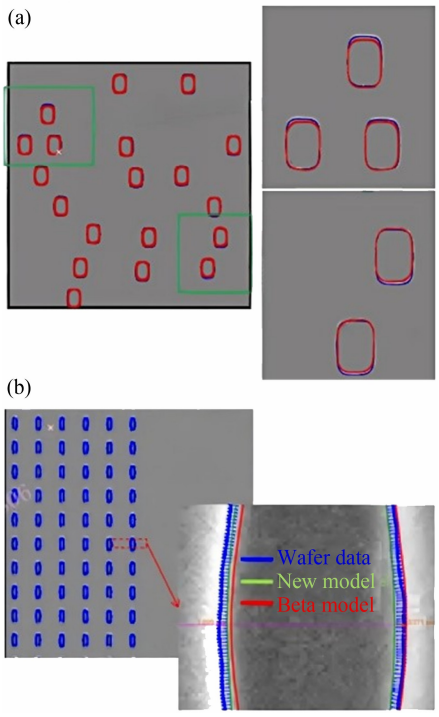

Fig. 5 Contour extraction and alignment with SEM image: (a) pattern shift averaged among contours, making the value inaccurate; (b) proper patterns with an anchor for alignment and accurate pattern shift extracted at edges.

are conducted to evaluate their performance relative to one another. To verify the capability of our modeling methodology, a beta model with only CD gauges is also calibrated.

4 Simulation results and wafer verification

Verification at the simulation level is performed on the CD and space gauges from design-like patterns. The design-like patterns are chosen by image-based pattern selection (IBPS) [30], which constructs feature vectors containing geometry and imaging information of the local structures to present typical patterns through the regression analysis. The typical patterns are extracted from actual designs, but OPC is performed with the beta model because the patterns are placed on the OPC test mask taped out previously. The wafer CD is collected on a CD uniformity wafer using the OPC test mask and averaged through 10 adjacent shots. The model error analysis of the verification data is shown in Fig. 6. The x axis denotes the number of specific gauges, and the y axis is the model error calculated by model CD minus wafer CD. The gauges are classified into two groups. The first one with most of the gauges marked in square blue dots is the CD gauge from design-like patterns, and the second one with fewer gauges marked in diamond purple dots is the space gauge, denoting the capability of capturing

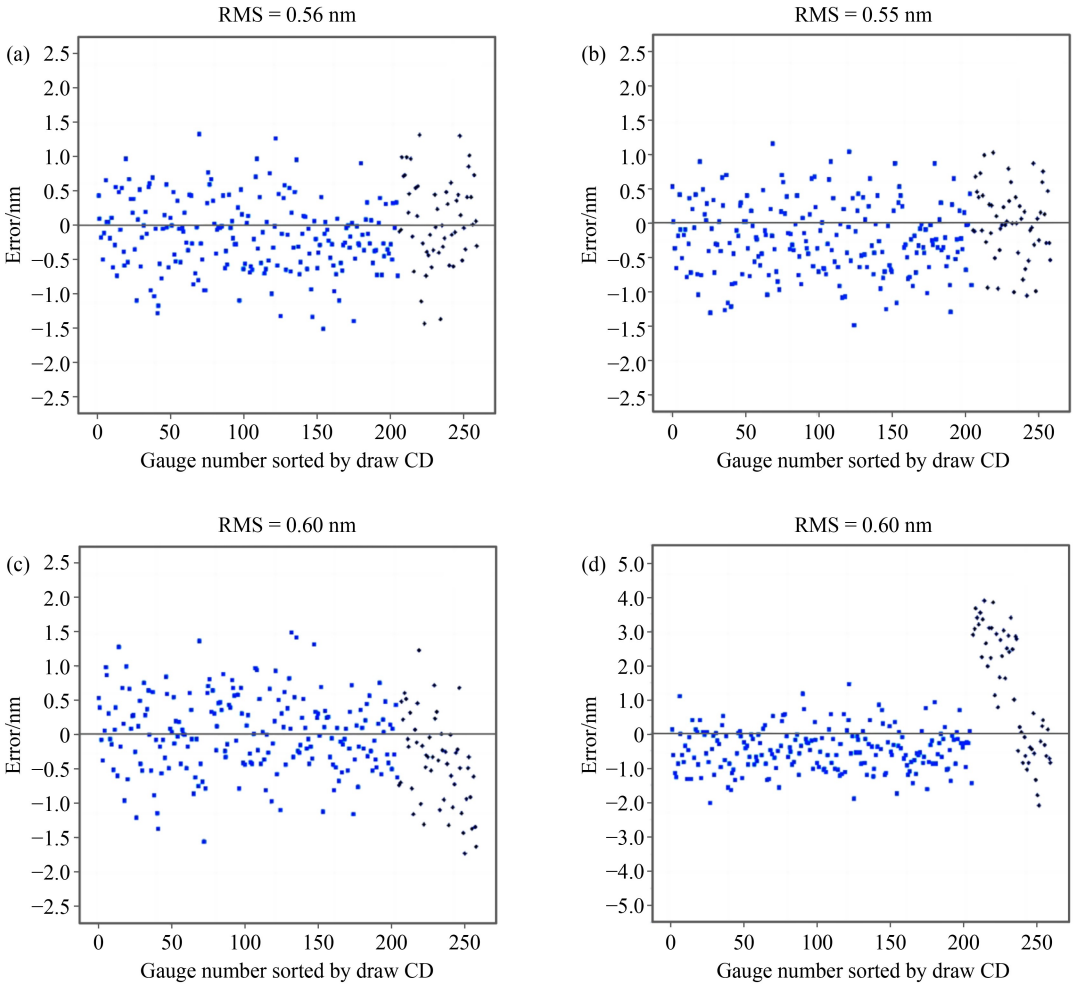

Fig. 6 Model error analysis on the same set of verification data: models from (a) classical genetic algorithm (GA) with gauges of critical dimensions (CDs) and spaces, (b) machine learning algorithm with the edge placement (EP) gauge, (c) classical GA with the EP gauge, and (d) beta model from only CD information.

pattern shift. Considering the CDs, the model error of all four models shows a range of around ±1.5 nm for all the gauges of verification, which is comparable with that of the beta model computed by only CD gauges.

Considering the spaces, several structures most frequently detected by IBPS with a dimension less than 600 nm are selected for verification against the beta model. The model error of space data shows excellent improvement from the three new models against the reference model. As mentioned above, the spaces of design-like patterns extracted from the SEM image may be averaged by adjacent structures on the image, which may perturb the measured pattern shift. Sequential measurement on adjacent pitches from a row of patterns is performed to measure the pattern shift more directly and precisely. The CD-SEM measures the pitch data with the same measurement settings as that for the measurement of CD. Due to similar model errors among the three new models, only the data of the classical model from the CD gauge are collected for analysis. The results are shown in Table 1. The comparison of simulation and wafer data shows a slight pitch error from the new model with a range of ±1 nm, while the beta model has a range of ±3.4 nm.

An actual production mask is then taped out based on the new model. Due to the similar performance of classical and ML models, the model calibrated based on CD and space gauges is used for the production mask to avoid potential overfitting issues. The selected layer from the actual chip is a via layer connecting upper and lower metal layers constructed by the self-aligned double patterning, which means the pitch of adjacent holes is the specific times of the minimum pitch restricted by metal layers. Moreover, the patterns are long-range ordering because of repeating functional cell arrays. Thus, all the pitches of structures within a cell array are measured sequentially from the left bottom to the top right. Then, all the measured pitches are grouped by the actual times of the minimum metal pitches for summary. The full-field inter- and intra-pattern shift data measured by the

distance between two adjacent holes from a batch of four wafers are collected and analyzed for a general, robust conclusion. The data from post OPC patterns by the beta model based on the same database are also collected for comparison. As shown in Fig. 7, the x axis is the distance of adjacent holes divided by the minimum pitch of lower metals, and the y axis is the bias of measured distance and designed distance. The statistical mean value and range are displayed. The new model with better prediction on pattern shift can reduce the range from around 9 to around 5 nm. The maximum mean value of the pattern shifts can be reduced from around 3.5 to within 1 nm. The global shift from zero bias is due to different magnification settings between the measurements and the OPC. The apparent rise from a slight to a large pitch is due to the distortion mentioned above of magnification. Minimal effort is devoted to the decomposition of systematic error from the data because it clearly shows the benefits of pattern-shift-aware modeling.

Table 1 Pattern shift error analysis on pitch measurement of sequential patterns from left to right within one row

Target pitch/nm	Wafer pitch/nm	Pitch error/nm	
		Beta model	New model
369	366.50	−2.55	0.19
369	367.10	−1.90	0.75
369	366.90	−2.00	0.51
328	325.00	−3.00	−0.42
533	536.30	3.30	0.78
328	324.60	−3.40	−0.78
533	536.14	3.14	0.62
328	325.77	−2.13	0.12
533	576.38	2.48	0.27
328	325.30	−2.50	−0.06
574	576.50	2.70	1.00
369	367.25	−1.65	0.48
369	367.73	−1.37	0.96

5 Conclusions

This work introduces efficient measurement and OPC modeling methods to address pattern shift issues in arbitrarily distributed hole layers caused by asymmetric aerial images from optical simulations. Conventional methods often overlook these pattern shifts. A set of test structures is designed to represent and measure the pattern shifts in our scenario accurately. Subsequently, the cost function of our OPC modeling is updated to emphasize the importance of the pattern shift by appropriately weighting test patterns in diverse groups. Our findings reveal that all the three calibrated models exhibit similar model errors, effectively capturing CDs and pattern shifts. This finding suggests that the pattern shift can be adequately captured through the SEM image contours and the well-designed and finely-tuned classical models. This outcome demonstrates the feasibility of acquiring a robust OPC model through traditional methods, mitigating the limitations associated with SEM contours and reducing the reliance on OPC tools' capabilities to handle SEM images or contours.

Nomenclature

Abbreviations

CD	Critical dimension
EP	Edge placement

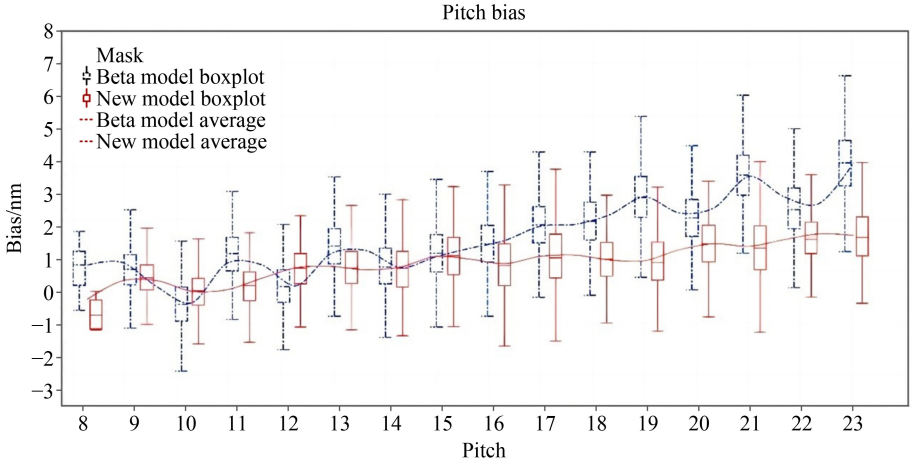

Fig. 7 Wafer verification data of pattern shift with a new mask from a batch of 4 wafers.

FOV	Field of view
IBPS	Image-based pattern selection
ML	Machine learning
OD	Optical diameter
OPC	Optical proximity correction
RET	Resolution enhancement technique
RMS	Root mean square
SEM	Scanning electron microscope
SRAF	Sub-resolution assist feature
TCC	Transmission cross-coefficient

Acknowledgements This work was funded by the National Natural Science Foundation of China (Grant Nos. 52130504, 52305577, and 52205592), the Key Research and Development Plan of Hubei Province, China (Grant No. 2022BAA013), the Major Program (JD) of Hubei Province, China (Grant No. 2023BAA008-2), the Innovation Projection of Optics Valley Laboratory, China (Grant No. OVL2023PY003), and the Postdoctoral Fellowship Program (Grade B) of the China Postdoctoral Science Foundation (Grant No. GZB20230244). The authors thank ASML BRION and HMI, the Netherlands, for the technical support from their engineers. The authors also acknowledge the experimental support from Fabs for the mask tape-out and wafer data collection.

Conflict of Interest The authors declare that they have no conflict of interest.

References

1. Wong A K. Resolution Enhancement Techniques in Optical Lithography. Washington: SPIE, 2001, 153–168
2. Ma X, Arce G R. Computational Lithography. New York: John Wiley & Sons, 2010, 10–17
3. Randall J, Gangala H, Tritchkov A. Lithography simulation with aerial image—variable threshold resist model. Microelectronic Engineering, 1999, 46(1–4): 59–63
4. Peng D, Hu P, Tolani V, Dam T, Tyminski J, Slonaker S. Toward a consistent and accurate approach to modeling projection optics. In: Optical Microlithography XXII. San Jose: SPIE, 2010, 7640: 76402Y
5. Liao H, Palmer S, Sadra K. Variable threshold optical proximity correction (OPC) models for high-performance 0.18-μm process. In: Optical Microlithography XIII. Santa Clara: SPIE Microlithography, 2000, 1033–1040
6. Roessler T, Frankowsky B, Toublan O. Improvement of empirical OPC model robustness using full-chip aerial image analysis. In: Proceedings of the 23rd Annual BACUS Symposium on Photomask Technology. Monterey: SPIE Photomask Technology, 2003, 5256: 222–229
7. Poonawala A, Milanfar P. Mask design for optical microlithography-an inverse imaging problem. IEEE Transactions on Image Processing, 2007, 16(3): 774–788
8. Ma X, Arce G R. Pixel-based OPC optimization based on conjugate gradients. Optics Express, 2011, 19(3): 2165–2180
9. Granik Y, Medvedev D, Cobb N. Towards standard process models for OPC. In: Proceedings of Optical Microlithography XX. San Jose: SPIE Advanced Lithography, 2007, 6520: 652043
10. Granik Y, Cobb N, Medvedev D. Extreme mask corrections: technology and benefits. In: Optical Microlithography XXI. San Jose: SPIE Advanced Lithography, 2008, 6924: 69243W
11. Bahnas M, Al-Imam M. OPC model calibration considerations for data variance. In: Optical Microlithography XXI. San Jose: SPIE Advanced Lithography, 2008, 6924: 69243U
12. Kusnadi I, Do T, Granik Y, Sturtevant J L, De Bisschop P, Hibino D. Contour based self-aligning calibration of OPC models. In: Metrology, Inspection, and Process Control for Microlithography XXIV. San Jose: SPIE Advanced Lithography, 2010, 7638: 76382M
13. Jayaram S, LaCour P, Word J, Tritchkov A. Model-based SRAF solutions for advanced technology nodes. In: Proceedings of SPIE 29th European Mask and Lithography Conference, 2013, 8886: 88860P
14. Zuniga C, Deng Y. Resist toploss modelling for OPC applications. In: Optical Microlithography XXVII. San Jose: SPIE Advanced Lithography, 2014, 9052: 905227
15. Taravade K N, Croffie E H, Jost A. Two-dimensional image based model calibration for OPC applications. In: Optical Microlithography XVII. Santa Clara: SPIE Microlithography, 2004, 1522–1527
16. Tabery C, Morokuma H, Matsuoka R, Page L, Bailey G E, Kusnadi I, Do T. SEM image contouring for OPC model calibration and verification. In: Optical Microlithography XX. San Jose: SPIE Advanced Lithography, 2007, 6520: 652019
17. Granik Y, Kusnadi I. Challenges of OPC model calibration from SEM contours. In: Metrology, Inspection, and Process Control for Microlithography XXII. San Jose: SPIE Advanced Lithography, 2008, 6922: 69221H
18. Filitchkin P, Do T, Kusnadi I, Sturtevant J L, De Bisschop P, Van de Kerkhove J. Contour quality assessment for OPC model calibration. In: Metrology, Inspection, and Process Control for Microlithography XIII. San Jose: SPIE Advanced Lithography, 2009, 7272: 72722Q
19. Hibino D, Shindo H, Abe Y, Hojyo Y, Fenger G, Do T, Kusnadi I, Sturtevant J L, De Bisschop P, Van de Kerkhove J. High accuracy OPC-modeling by using advanced CD-SEM based contours in the next generation lithography. In: Metrology, Inspection, and Process Control for Microlithography XXIV. San Jose: SPIE Advanced Lithography, 2010, 7638: 76381X
20. Kim Y, Lee S, Hou Z, Zhao Y, Liu M, Zheng Y, Zhao Q, Kang D, Wang L, Simmons M, Feng M, Lang J, Choi B, Kim G, Sim H, Park J, Yoo G, Lee J, Ko S, Choi J, Kim C, Park C. OPC model accuracy study using high volume contour based gauges and deep learning on memory device. In: Metrology, Inspection, and Process Control for Microlithography XXXIII. San Jose: SPIE Advanced Lithography, 2019, 10959: 1095913
21. Weisbuch F, Jantzen K. Enabling scanning electron microscope contour-based optical proximity correction models. Journal of Micro/Nanolithography, MEMS, and MOEMS, 2015, 14(2): 021105
22. Fischer D, Han G, Oberschmidt J, Cheng Y W, Maeng J Y, Archie C, Lu W, Tabery C. Challenges of implementing contour modeling

in 32 nm technology. In: Metrology, Inspection, and Process Control for Microlithography XXII. San Jose: SPIE Advanced Lithography, 2008, 6922: 69220A

23. Chuyeshov C, Carrero J, Sezginer A, Kamat V. Calibration of e-beam and etch models using SEM images. In: Photomask Technology. Monterey: SPIE, 2009, 7488: 74883I
24. De Bisschop P, Van de Kerkhove J. Alignment and averaging of scanning electron microscope image contours for optical proximity correction modeling purposes. Journal of Micro/Nanolithography, MEMS, and MOEMS, 2010, 9(4): 041302
25. Hopkins H H. The concept of partial coherence in optics. Proceedings of the Royal Society of London Series A: Mathematical and Physical Sciences, 1951, 208(1093): 263–277
26. Drozdov A N, Kempsell M L, Granik Y. Fitness and runtime correlation of compact model complexity. In: Optical Microlithography XXI. San Jose: SPIE Advanced Lithography, 2008, 6924: 692445
27. Kumar P, Srinivasan B, Mohapatra N R. Fast and accurate lithography simulation using cluster analysis in resist model building. Journal of Micro/Nanolithography, MEMS, and MOEMS, 2015, 14(2): 023506
28. Yuan W, Lu Y, Zhao Y, Chen S, Li M, Hu H, Yao S, Liu Z, Li Q, Tian Y, Zhou Z, Gu L, Wang J, Sheng X, Yan G, Zheng Y, Yao Y, Xiao Y, Liu L, Zhao Q, Feng M, Chen J, Lang J. Metrology and deep learning integrated solution to drive OPC model accuracy improvement. In: Optical Microlithography XXXII. San Jose: SPIE Advanced Lithography, 2019, 10961: 109610N
29. Watanabe Y, Kimura T, Matsunawa T, Nojima S. Accurate lithography simulation model based on convolutional neural networks. In: Proceedings of the XXIV Symposium on Photomask and Next-Generation Lithography Mask Technology. Yokohama: SPIE, 2017, 10147: 104540I
30. Sun R, Kang D, Jia C, Liu M, Shao D, Kim Y, Shin J, Mark S, Zhao Q, Feng M, Zhao Y, Wang S, Kim S, Ko S, Kim S, Choi J, Park C. Enhancing model accuracy and calibration efficiency with image-based pattern selection using machine learning techniques. In: Optical Microlithography XXXIV. San Jose: SPIE Advanced Lithography, 2021, 11613: 116130Y